

NASA/TM—1999-209394



Application of the RNS3D Code to a Circular-Rectangular Transition Duct With and Without Inlet Swirl and Comparison With Experiments

Richard H. Cavicchi
Glenn Research Center, Cleveland, Ohio

National Aeronautics and
Space Administration

Glenn Research Center

October 1999

This report is a formal draft or working paper, intended to solicit comments and ideas from a technical peer group.

This report contains preliminary findings, subject to revision as analysis proceeds.

Available from

NASA Center for Aerospace Information
7121 Standard Drive
Hanover, MD 21076
Price Code: A03

National Technical Information Service
5285 Port Royal Road
Springfield, VA 22100
Price Code: A03

Application Of The RNS3D Code To A Circular-Rectangular Transition Duct With And Without Inlet Swirl And Comparison With Experiments

Richard H. Cavicchi
National Aeronautics and Space Administration
Glenn Research Center
Cleveland, Ohio 44135

Summary

Circular-rectangular transition ducts are used between engine exhausts and nozzles with rectangular cross sections that are designed for high performance aircraft. NASA Glenn Research Center has made experimental investigations of a series of circular-rectangular transition ducts to provide benchmark flow data for comparison with numerical calculations. These ducts are all designed with superellipse cross sections to facilitate grid generation. In response to this challenge, the three-dimensional RNS3D code has been applied to one of these transition ducts. This particular duct has a length-to-inlet diameter ratio of 1.5, and an exit-plane aspect ratio of 3.0. The inlet Mach number is 0.35. Two GRC experiments and the code were run for this duct without inlet swirl. One GRC experiment and the code were also run with inlet swirl. With no inlet swirl the code was successful in predicting pressures and secondary flow conditions, including a pair of counter-rotating vortices at both sidewalls of the exit plane. All these phenomena have been reported from the two GRC experiments. However, these vortices were suppressed in the one experiment when inlet swirl was used; whereas the RNS3D code still predicted them. The experiment was unable to provide data near the sidewalls, the very region where the vortices were predicted.

Introduction

Rectangular exhaust nozzles are used in high performance aircraft to enhance maneuverability and performance. In such an aircraft, a transition duct is needed between the circular engine exhaust and the rectangular nozzle inlet. A tradeoff arises between aircraft performance and the additional weight of a transition duct. Of equal or greater concern, however, is the potential for stagnation pressure loss that may be incurred by the changing shape of the duct.

NASA Glenn Research Center has conducted experimental investigations of circular-rectangular transition ducts as a means of validating three-dimensional computer codes. In response to this challenge, the current study uses the three-dimensional RNS3D code, documented in reference 1, to obtain computational results for a circular-rectangular duct. In changing from a circular to a rectangular cross section, the walls on two sides of the duct diverge; while the opposite walls converge. Pressure gradients of opposite sign occur, inducing secondary flows that lead to potential vortex formation.

Investigations have been made at GRC by both experiment and the current computations for a transition duct with and without inlet swirl. Ostensibly, such a duct's design should attempt to minimize transverse velocity components at the duct's exit and total pressure loss in the duct. However, turbine exit flow may contain a significant rotational component, known as inlet swirl, in the duct. At turbine off-design conditions, the swirl angle may exceed 30° . Nevertheless, there may be certain beneficial aspects to swirling flow. Having a radial velocity component within the duct during transition helps the flow follow the steep sidewall slopes. Furthermore, swirling the flow can help reduce jet exhaust noise, as it increases the rate of decay of the jet axial velocity. However, reference 2 reveals that nozzle thrust ratio is reduced with increase of swirl angle for fully choked flow.

Configuration

Several circular-rectangular transition ducts have been designed at GRC. The cross sections of these ducts are defined by superellipses to ease grid generation in computational investigations. The coordinates of the duct used in the current study are presented in reference 3. An isometric view showing one-half of this duct

appears in figure 1(a), which depicts a $21 \times 20 \times 86$ grid. Figure 1(a) shows a constant-shape section attached to the transition duct exit. The length of the transition region itself is 1.5 times its inlet diameter. The appended constant-shape section shown in figure 1(a) is 2.0 inlet diameters long. Hence, the overall L/D is 3.5. The aspect ratio of the exit rectangular cross section is 3.0. That is, the long side of the rectangle is three times the short side. The cross sectional area of the transition region increases to 1.15 times its inlet value during the first half of its length; then it decreases back to the inlet value during the last half. One-half of the exit cross section showing the 21×20 grid used herein appears in figure 1(b). Figure 1(c), taken from reference 4, shows a drawing of the duct with its constant-area section attached. The xyz axes are also shown in this figure. The $21 \times 20 \times 86$ grid denotes the number of points in the z-, y-, and x-directions, respectively. Because, reference 4 took data at 4 planes, this computational study presents results at these same planes, which correspond to axial grid point stations 29, 37, 46, and 74.

Inlet Flow Conditions

The inlet flow conditions used in the computations are presented in table I. They are identical to those specified in the experimental tests of reference 4. The Mach number is 0.35. The Reynolds number without inlet swirl is 1,547,000. This Reynolds number is based on the centerline velocity and the inlet diameter. The Reynolds number for the case using inlet swirl is 1,366,000. Inlet swirl angles of 15.6° (as used in ref. 4) and 45° are used in the computations. The value of 45° was arbitrarily chosen as an upper extreme value.

Features Of The RNS3D Code

The following summary briefly describes the ingredients of the RNS3D code. The analysis and methods used in its derivation are described in great detail in reference 1.

The steady compressible Navier-Stokes equations were approximated to yield a set of Governing equations. Inherent in this procedure were the following three assumptions.

- (1) The flow consists of a primary (streamwise) flow and a secondary (transverse) flow.
- (2) The pressure field can be represented by a three-dimensional known field, as coming from a three-dimensional potential flow analysis plus a one-dimensional correction for viscous blockage and pressure loss.
- (3) Second derivatives in the marching direction are negligible.

The Governing equations were replaced by implicit Finite Difference approximations with accuracy $O(\Delta x, \Delta y, \Delta z)$.

A mixing length eddy-viscosity turbulence model was used in this study.

The boundary conditions used were no-slip adiabatic walls for solid surfaces.

Table II presents the first part of the program to display the values of the code settings used in the current calculations. These parameters are described in reference 1.

Results And Discussion

No Inlet Swirl

Results of the current computations without inlet swirl will be compared with the experimental results of references 3 and 4. As in reference 4, static and stagnation pressure coefficients will be referred to herein merely as static and stagnation pressures, respectively.

Static pressure.—Reference 4 uses static pressure as a basis for explaining secondary flow effects. Figure 2 displays the axial variation of the surface value of static pressure along the dashed line of figure 1(c), at the end of the z-axis. The circles present the experimental results of reference 4; whereas the results calculated from the RNS3D code are shown by the solid curve. The dashed vertical lines in figure 2 depict the 4 axial planes of the cross stream measurements denoted in figure 2(c).

Figure 2 reveals that the code correctly predicts the static pressure distribution throughout most of the circular-rectangular transition section itself. The flow field that occurs outside the boundary layer in response to the changing duct geometry is a primary cause of static pressure variation. The change in the duct cross

section causes the flow to converge in the xz -plane, and to diverge in the xy -plane. The entering flow is parallel to the x -axis. As the wall diverges in the y -direction, it deflects the flow away from the x -axis in the xy -plane. Meanwhile, convergence of the wall in the z -direction deflects the flow towards the x -axis in the xz -plane. This behavior, accompanied by a change of sign of the radius of curvature, yields minimum static pressure near either end of the y -axis, and maximum near either end of the z -axis. This observation explains why the spike peaks occur in figure 2 at the end of the z -axis in the vicinity of plane 1. Recall that this figure pertains to the surface.

Farther downstream in the constant-area section following the transition, the walls force the flow back to a direction more nearly parallel to the x -axis. The static pressure distribution there is thus the reverse of that discussed at plane 1. This reasoning explains the steep drop from the peaks in figure 2. However, in the straight section appended to the transition duct, the solid curve continues a downward trend; whereas the circles display a leveling off of the static pressure. Nevertheless, RNS3D calculations (not presented herein) are more in agreement in the appended straight section for lower Mach and Reynolds numbers.

Static pressure contours are presented in figures 3(a) to (c) for the computed and experimental results. Figure 3(a) displays that the maximum values occur at plane 1 at the end of the z -axis. This observation is confirmed by the experimental results in figure 3(b) at plane 1. Planes 3 and 4 of figure 3(a) show maximum static pressure at the end of the y -axis, and minimum at the end of the z -axis. This lowering of the pressure at the end of the z -axis is also shown beyond the spikes peaks in figure 2. Figure 3(c) of reference 4 also shows maximum pressure at plane 3 to be at the end of the y -axis. Furthermore, the isometric plot of figure 4 gives a graphic view of the surface static pressure reaching a maximum in the transition region, and then diminishing in the exit section. References 3 and 4 both verify this static pressure reversal behavior. Finally, figure 5 is presented to show the computed static pressure distribution along the duct periphery at the four axial plane locations. Figure 5 displays high transverse pressure gradients at planes 1 and 2. These gradients induce lateral skewing of the near wall flow in the vicinity of the sidewall (at the end of the y -axis). This secondary flow, which in turn distorts the primary flow, will be discussed subsequently.

Axial velocity.—The axial velocity components computed in this study are presented in figure 6(a). At plane 1, which is early in the transition, the boundary layers on all walls are very thin. A small increase in this thickness due to natural buildup appears at plane 2. Subsequently, at planes 3 and 4, the region of mainstream flow has greatly diminished as the result of secondary flow caused by the static pressure distribution previously discussed. The axial velocity contours of figure 6(a) are confirmed by the experimental contours of figure 6(b) of reference 4. However, the axial velocity contours of figure 6(a) more closely resemble the experimental results presented in reference 3 and shown here in figure 6(c).

Transverse velocity.—The transverse velocities (secondary flow) are presented in figure 7. The cross flow velocities (magnitude of the y - and z -components) are in figure 8. These velocities are all zero at the duct inlet. Their buildups in planes 1 to 4 arise from the effect of the duct's changing configuration on the transverse static pressure gradients, as discussed earlier. Clearly evident in planes 3 and 4 in figure 7(a) is a pair of counterrotating sidewall vortices, as verified in references 3 and 4. A pair of vortices also appears in the cross flow velocity plots of figure 8. Note that the vortices in plane 4 of figure 8 are more nearly circular than in plane 3.

Stagnation pressure.—Computed contours of stagnation pressure are shown in figure 9(a). At plane 1 the contours, for the most part, follow the shape of the periphery. At plane 2, secondary flow and viscous effects are evident in the sidewall region. These effects produce larger regions of stagnation pressure loss at planes 3 and 4, as even the long walls' areas are affected. Again, these results are confirmed by the experimental plots of references 4 and 3 that appear herein in figures 9(b) and (c), respectively.

Axial component of vorticity.—The axial component of vorticity results are presented by way of figure 10. In reference 5 Shapiro explains how a bend in a pipe causes a buildup of vorticity. A transition duct, although not strictly a bend, has some similar characteristics. For example, the streamlines in a transition duct curve to conform with the changing shape of the duct. According to Shapiro, an entering nonuniform, but axial flow has an incoming axial component of vorticity, given by

$$\omega_y = -\frac{\partial u}{\partial z}$$

As the streamlines follow an angle θ , a secondary vorticity ω_{sec} is induced, which is a new axial component. Shapiro shows that

$$\omega_{sec} = 2 \omega_y \theta$$

He further shows that this secondary component ω_{sec} produces a swirling component of velocity V_s near the walls. By use of Stokes' theorem, he finally shows that

$$V_s \equiv \left(\frac{\theta}{2}\right) h\omega_y$$

where h is the duct height.

The previous discussion pertains to a situation without inlet swirl. When inlet swirl is applied, the secondary flow velocity V_s augments the transverse velocity that would occur without swirl.

In the first half of the transition duct, the transverse static pressure gradients of figure 5 coupled with the area increase induce the vorticity shown at planes 1 and 2. At plane 3 the static pressure distribution has reversed and the area has decreased, which produce the sidewall counter-rotating vortices appearing at planes 3 and 4. These vortical patterns were also found experimentally by references 4 and 3, and are presented herein as figures 10(b) and (c), respectively. It would be desirable if these vortices could be avoided, as they cause the large regions of stagnation pressure loss observed in figure 9. However, this is part of the tradeoff in transitioning from a circular to a rectangular cross section.

With Inlet Swirl

Results of the current computations using inlet swirl will be compared with the experimental results of reference 4 (with swirl) and with the computational results of the previous section (no swirl).

Static pressure.—Figure 11 presents the axial variation of static pressure when inlet swirl was used. The circles depict the experimental data of reference 4 for 15.6° inlet swirl. The solid and dotted curves represent the calculated values for 15.6° and 45° inlet swirl, respectively. As in figure 2 (without swirl), the calculated results with swirl of figure 11 show good agreement with the experimental data throughout most of the transition section. Again, in the appended straight section the calculated static pressure continues to decrease; whereas the experimental values level off.

Static pressure contours are presented in figures 12(a) and (b) for the computed and experimental results, respectively. Figure 12(a) discloses that the maximum values occur at plane 1 at the end of the z -axis, as was calculated for no inlet swirl earlier. Plane 1 of the experimental results of figure 12(b) shows that maximum pressure occurs at the sidewall on one side of the y -axis, and minimum pressure occurs on the other side. This is a decided difference from figure 12(a). Maximum pressure remains near the z -axis at planes 2 and 3 in figure 12(a). Maximum pressure finally appears at the sidewall at plane 4, as was found in the calculated no-swirl results previously.

Figure 13 presents an isometric view of the calculated results for static pressure. This figure shows vividly that maximum static pressure in the duct occurs in the region of plane 4 at the z -axis extremities. Finally, figure 14 displays the computed static pressure distribution along the duct periphery at the four axial plane locations. The primary difference between figures 5 and 14 is the higher value of the pressure profile at plane 2 with inlet swirl. This observation implies that the presence of swirl reduces the viscous losses and accompanying boundary layer growth.

Axial velocity.—Figure 15 presents axial velocity contours at planes 1 to 4 for flow with 15.6° inlet swirl. Computed results appear in figure 15(a) and experimental results are in figure 15(b). Skewing of the contour lines is evident in both of these plots in response to the inlet swirl. This effect persists throughout the axial length of the duct. As expected, the skewing effect is greater for 45° inlet swirl than for 15.6° . However, the region of mainstream maximum velocity is about the same for both swirl angles.

Transverse velocities.—Contours of the y -component of velocity are presented in figures 16(a) and (b) for the computed and experimental results, respectively. A pair of counter-rotating sidewall vortices has already appeared at plane 2 for the calculated results of figure 16(a). They become more pronounced in planes 3 and 4. This observation is found for both 15.6° and 45° inlet swirl. The experimental results shown in figure 16(b) show no evidence of these vortices at any plane. Both references 3 and 4 as well as the previous section reported such vortices for flow without inlet swirl, however. Note that no experimental data are presented immediately adjacent to the sidewall in figure 16(b). Reference 4 states that this location was out of the measurement region. Thus, it appears that more experimental work should be done for flow with inlet swirl.

Calculated cross flow velocity contours appear in figure 17. The characteristics of figure 17 differ from those in figure 16(a) only to a minor extent. Therefore, the same comments apply.

Stagnation pressure.—Figures 18(a) and (b) present stagnation pressure contours for the computed and experimental results, respectively. The slight distortion displayed at plane 1 of figure 18(a) becomes progressively more pronounced at planes 2 to 4. The experimental results of figure 18(b) reveal a smaller effect of the swirling inlet flow.

Axial component of vorticity.—The axial component of vorticity is shown in figures 19(a) and (b) for the current calculated results and the experimental results of reference 4, respectively. Planes 3 and 4 of figure 19(a) display a calculated pair of sidewall vortices; whereas the experimental results of figure 19(b) do not show sidewall vortices. In fact, reference 4 states “For the inlet swirl case studied, the sidewall vortices were not observed. The static pressure distribution was altered by the swirling velocity flow to an extent that the sidewall vortices were suppressed.”

Computations using inlet swirl at 45° also predicted a pair of exit sidewall vortices. Thus, the hoped for and expected elimination of sidewall vortices by using inlet swirl did not occur in the computations. These vortices are associated with the derogatory effect of the stagnation pressure loss. As noted previously, reference 4 does not present near sidewall results because this region is out of the experimental range.

Concluding Remarks

Results from application of the three-dimensional RNS3D code to a circular-rectangular transition duct without inlet swirl displayed fair agreement with those obtained experimentally by two different GRC groups. These results pertain to static and stagnation pressures, axial velocity, secondary velocity, and axial vorticity. It is particularly significant that the code predicts a pair of counter-rotating vortices at the sidewalls, as both experiments had found.

However, agreement was not so close when inlet swirl was applied. The experimental results revealed that the pair of exit counter-rotating sidewall vortices was suppressed with the use of inlet swirl; whereas they persisted in the RNS3D studies. Nevertheless, due to measurement restrictions, the experimental work was unable to provide data adjacent to the sidewall, the very region where the vortices were predicted to occur. This discrepancy implies that additional experimental work with inlet swirl is needed. Furthermore, application of other numerical codes to this duct with inlet swirl should provide deeper insights.

References

1. Towne, C.E.: “RNS3D User's Guide,” version 0.9. NASA GRC. Mar. 1995.
2. Burley, J.R., II, and Carlson, J.R.: “Circular-To-Rectangular Transition Ducts For High-Aspect Ratio Non-Symmetric Nozzles.” AIAA Paper 85-1346. 1985.
3. Davis, D.O.: “Experimental Investigation of Turbulent Flow Through a Circular-Rectangular Transition Duct,” NASA TM-105210, Sep. 1991.
4. Reichert, B.A., Hingst, W.R., and Okishi, T.H.: “An Experimental Comparison of Nonswirling and Swirling Flow in a Circular-Rectangular Transition Duct,” NASA TM-104359, Jan. 1991.
5. Shapiro, A.H.: “Fluid Dynamics,” Vol. III. “Deeper Insights.” Video Course Material, M.I.T., 1984.

TABLE I.—INLET FLOW CONDITIONS

| | No inlet swirl | With inlet swirl |
|--------------------------|----------------|------------------|
| Centerline Mach number | 0.35 | 0.35 |
| Reynolds number | 1,547,000 | 1,366,000 |
| Boundary layer thickness | 0.08014 | 0.20484 |
| Inlet swirl angle | 0 | 15.6° |
| | | 45.0° |

TABLE II.—A PORTION OF RNS3D CODE TO PRESENT CODE SETTINGS

```

#! /bin/sh
#
# crvi21- RNS3D case of viscous flow in a circular-to-rectangular
# transition duct
#
# To run: ./crvi21 >& crvi21.sgi
#
# AUTHOR: Dick Cavicchi
# Date: 05-15-99

set -x

# Set up and link necessary input/output files

touch crvi21.plot35x
touch crvi21.plot35q
touch /usr/tmp/sc9
touch /usr/tmp/restrt
touch /usr/tmp/sc15
touch /usr/tmp/sc20
ln -s crvi21.plot35x fort.7
ln -s crvi21.plot35q fort.8
ln -s /usr/tmp/sc9 fort.9
ln -s /usr/tmp/restrt fort.11
ln -s /usr/tmp/sc15 fort.15
ln -s /usr/tmp/sc20 fort.20
ln -s cc.bpflow fort.13

# Run code

/usr/grc/fscavch/pg/pg09/pg09.ex << EOD
1Circular Inlet, Geometry
&restrt
 irstot=21 ,
&end
&fluids
cmach=.35, rey=1547000., bld(4)=.08014,
t=-1.0, dt=0.1,
ns=21,
ney=21, nez=20,
iplot=2, icoef(1,3)=2500, icoef(1,5)=300,
icoef(1,9)=1, icoef(2,3)=-1, kturb=1,
iwsta=1,21,29,37,46,86,
&end
&geom
ipb=3, vis=.15,
pcl=33*0., pfw=154*0.,
pcl(2,3)=1., ngeom=3,
pgeo(1,1)=1., pgeo(1,2)=1., pgeo(1,4)=2.,
&end
&vortex
zzr=-0.5, zzi=0.5, rcore=0.25, qtedge=0.0,
&end

```

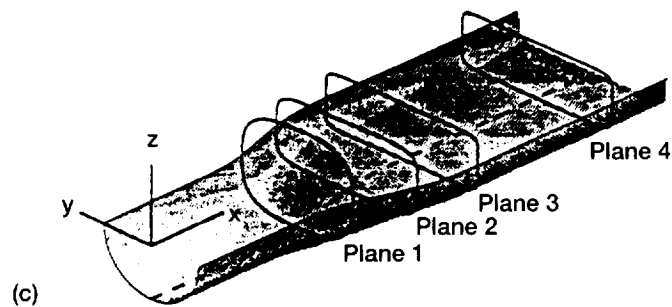
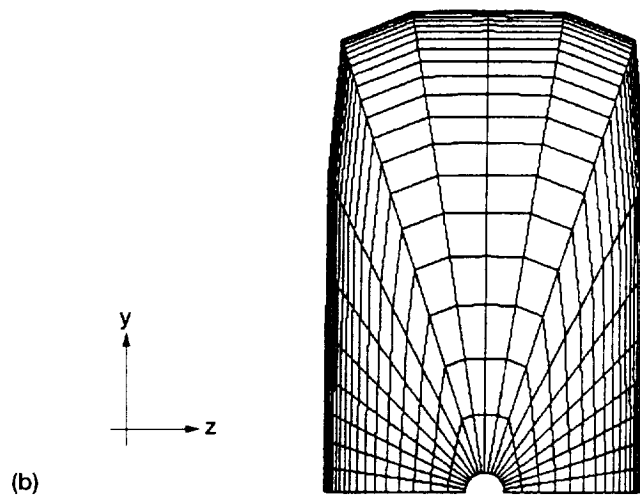
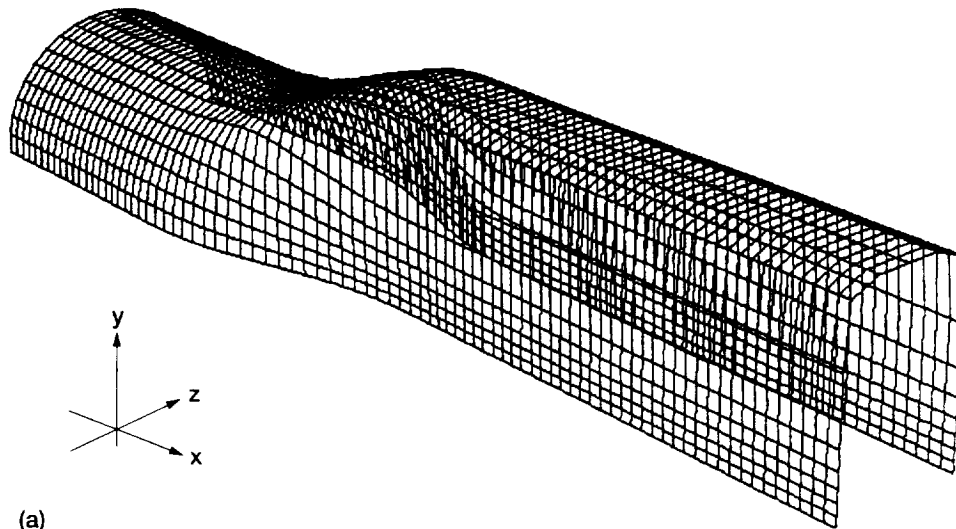


Figure 1.—Circular-to-rectangular transition duct. (a) Isometric side half 21x20x86. (b) Exit cross section 21x20. (c) Lower half.

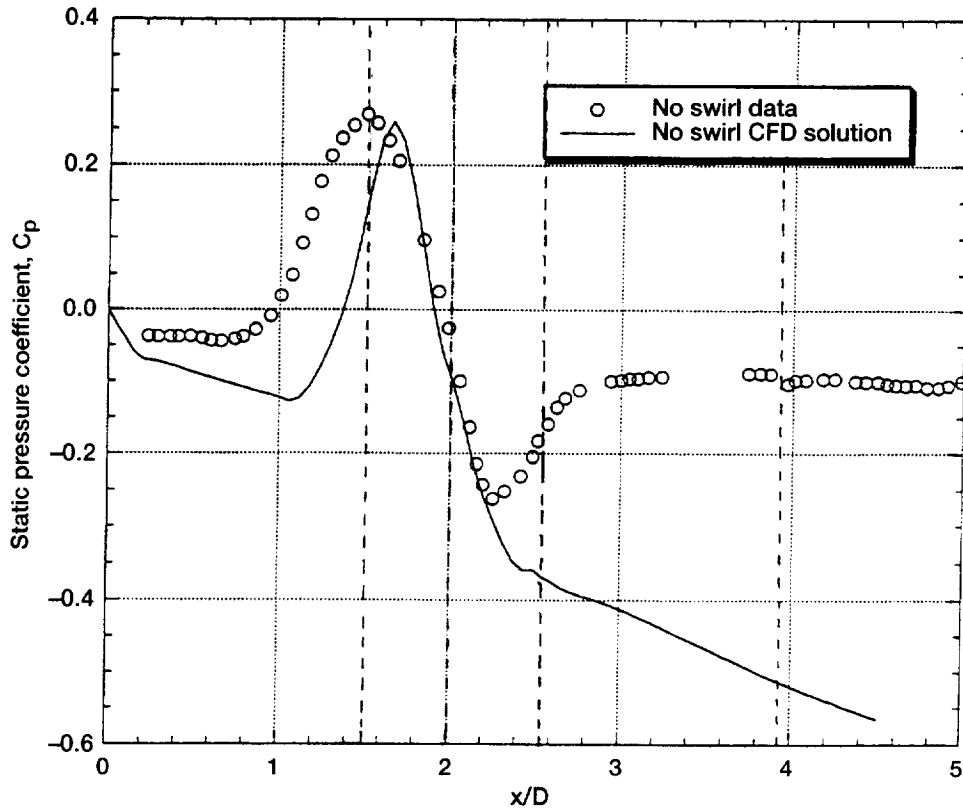


Figure 2.—Axial variation of static pressure coefficient.

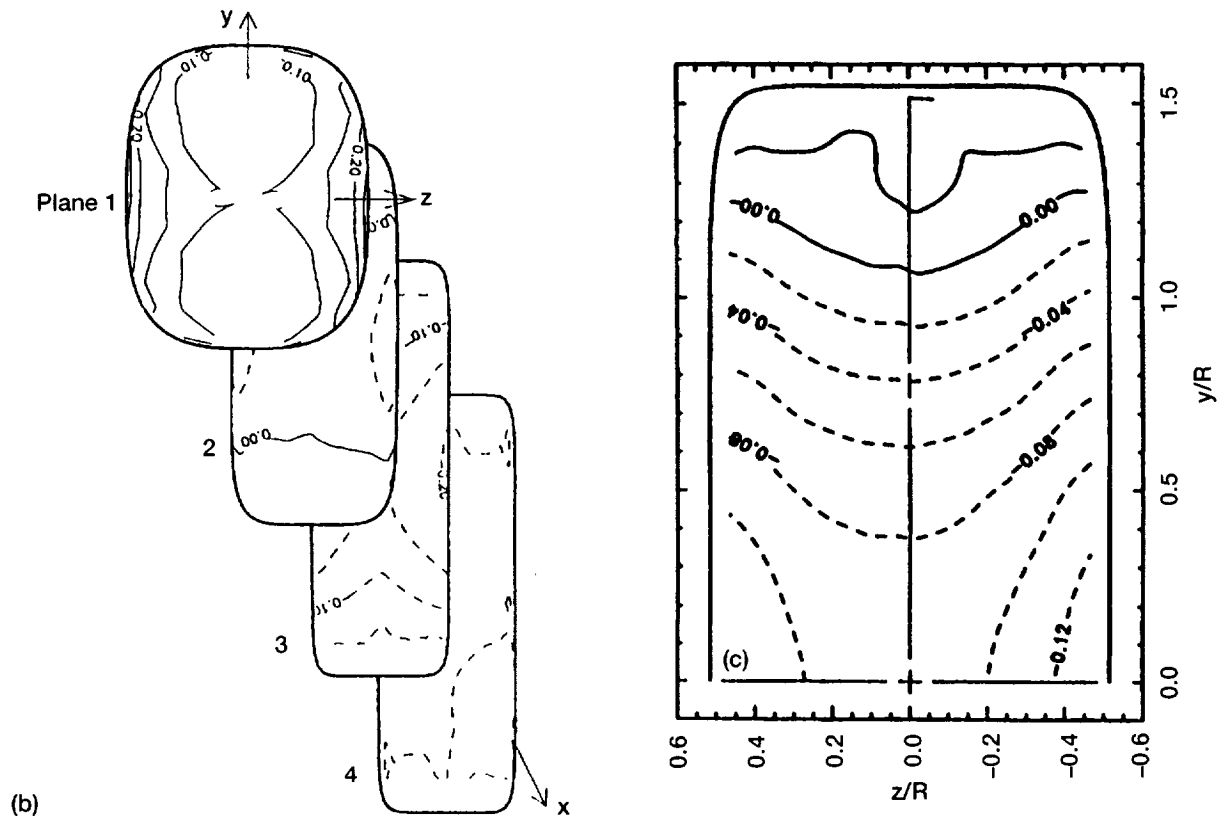
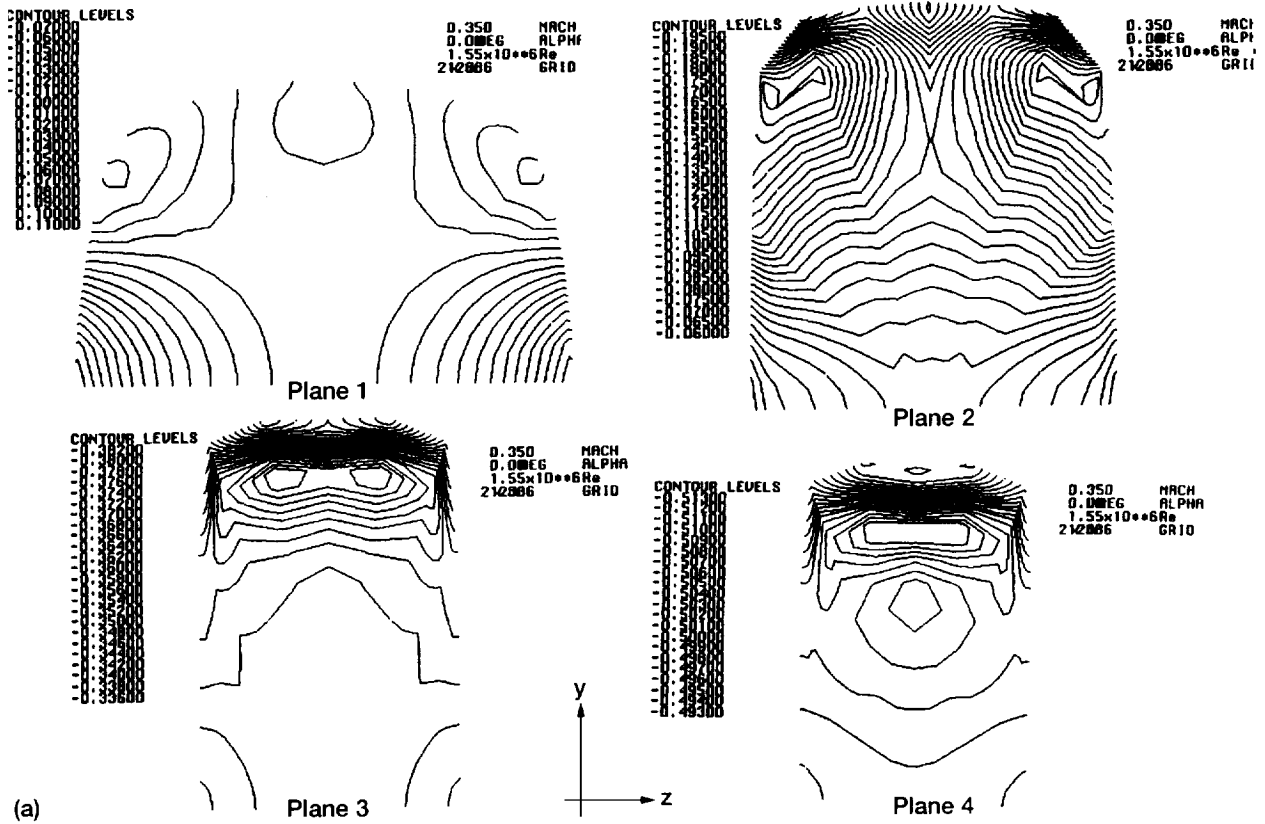


Figure 3.—Static pressure coefficient. (a) Calculated results. (b) Experimental results (ref. 4). (c) Experimental results (ref. 3) for Plane 3.

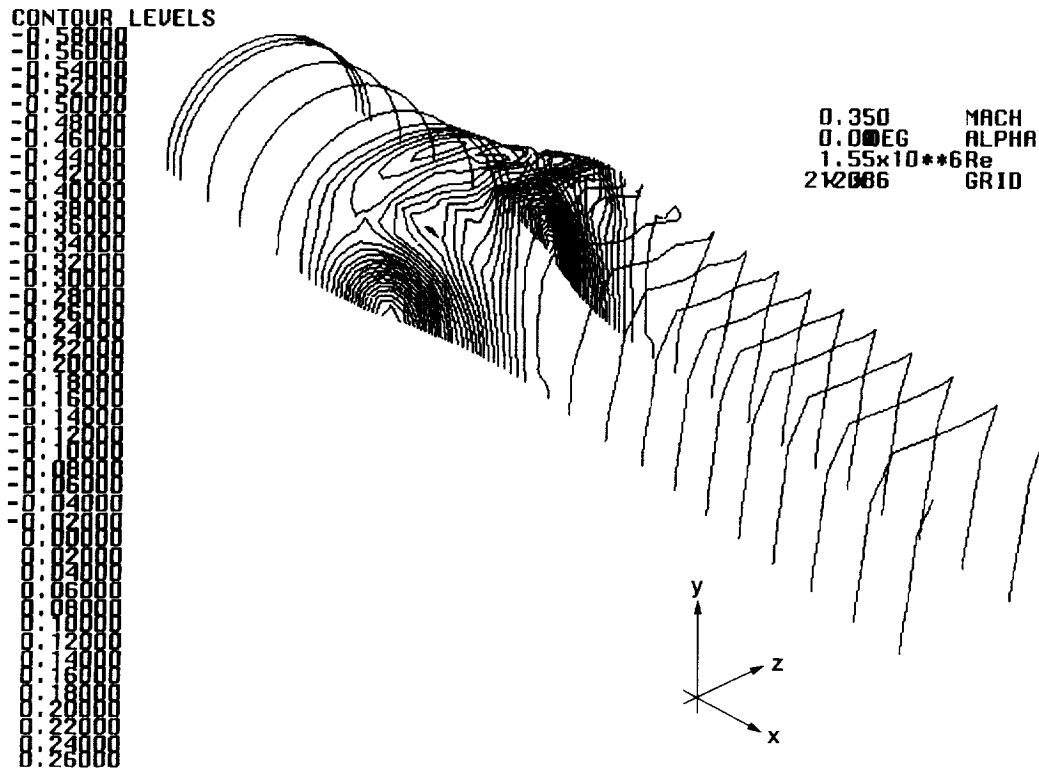


Figure 4.—Isometric view of static pressure coefficient, calculated results.

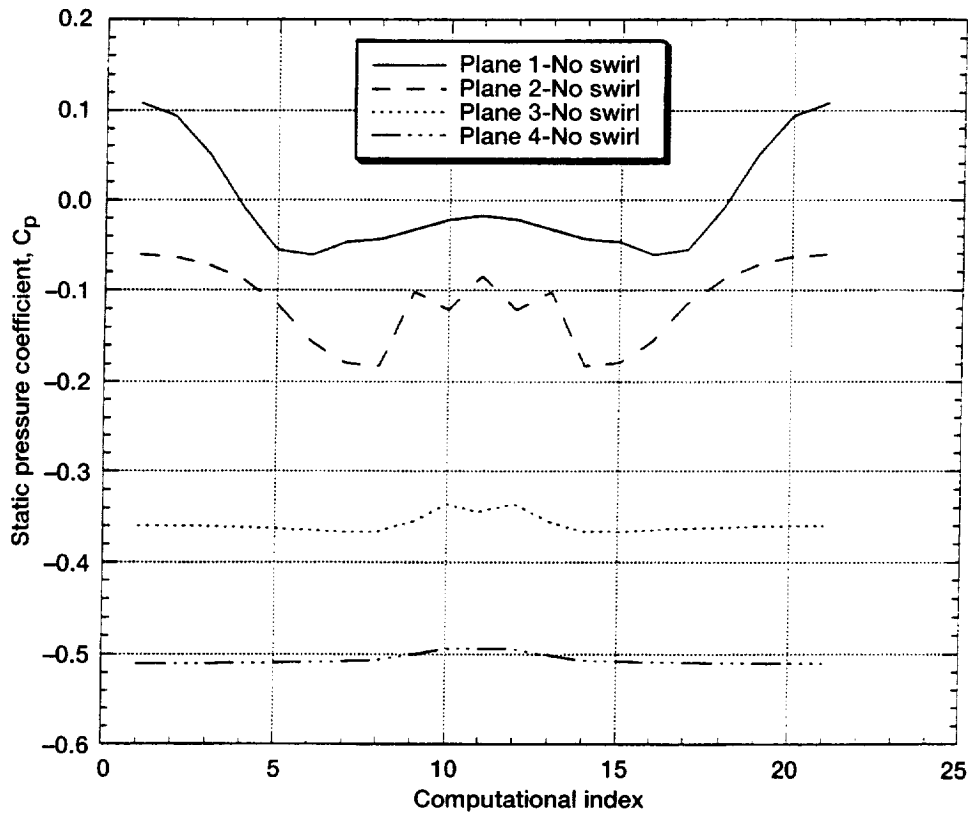
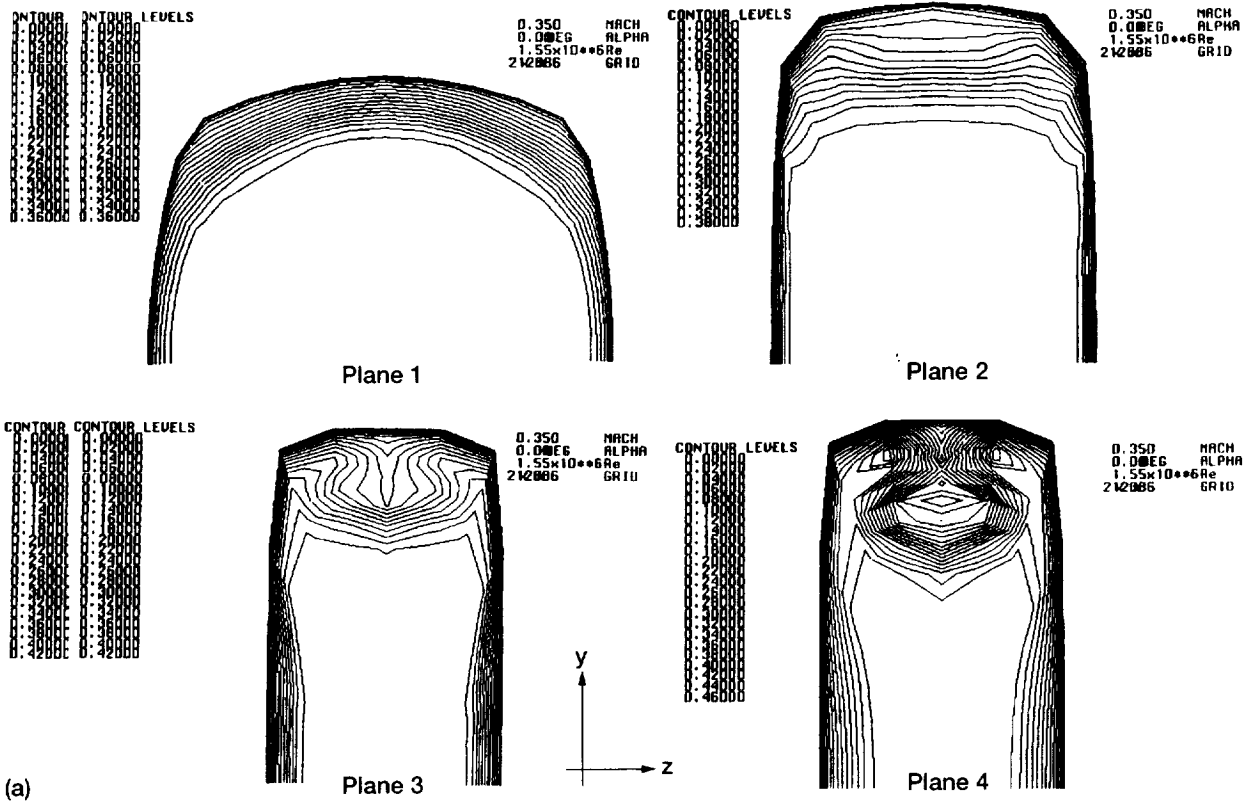
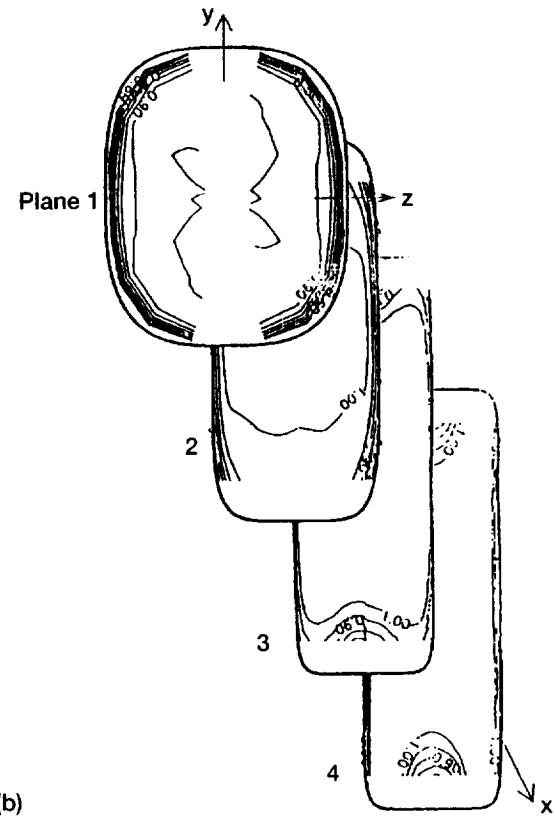


Figure 5.—Peripheral variation of static pressure coefficient.



(a)



(b)

Figure 6.—Axial velocity. (a) Calculated results. (b) Experimental results (ref. 4).

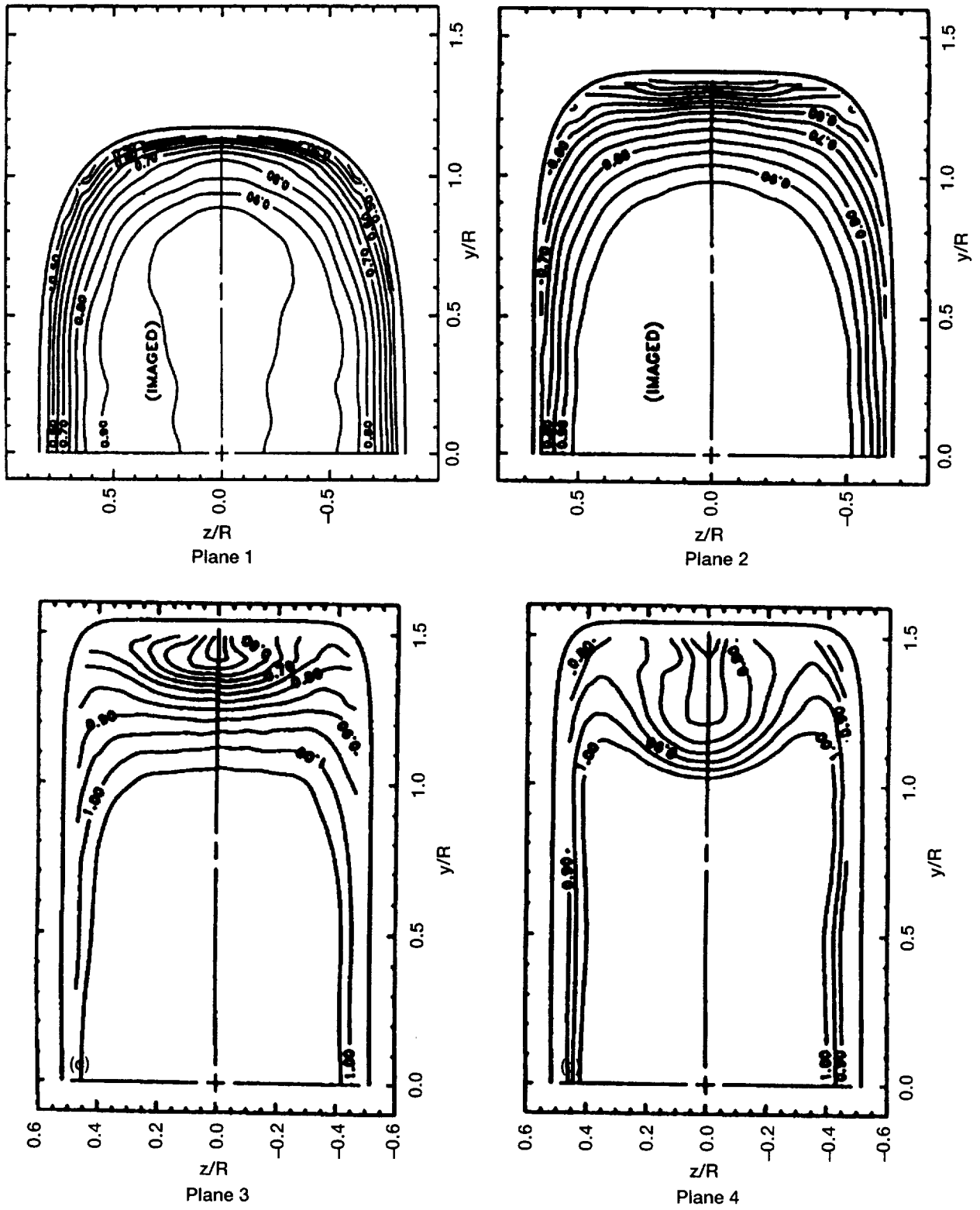


Figure 6.—Concluded. (c) Experimental results (ref. 3).

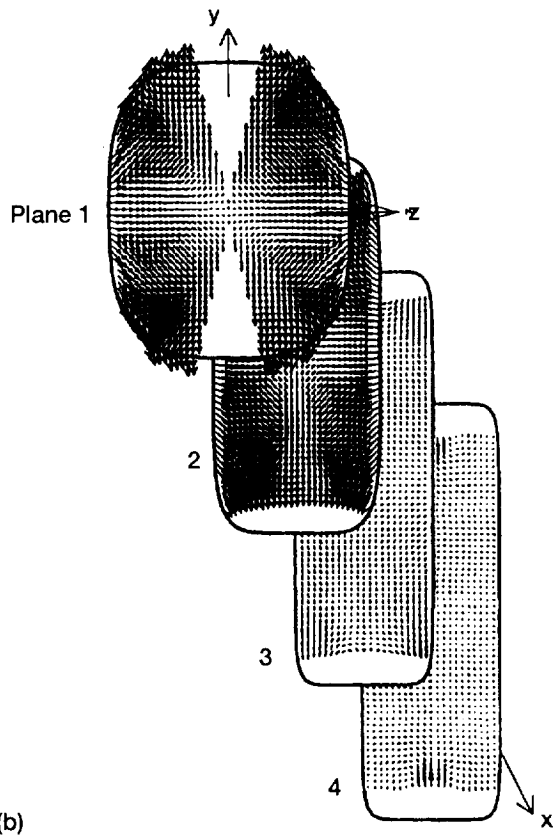
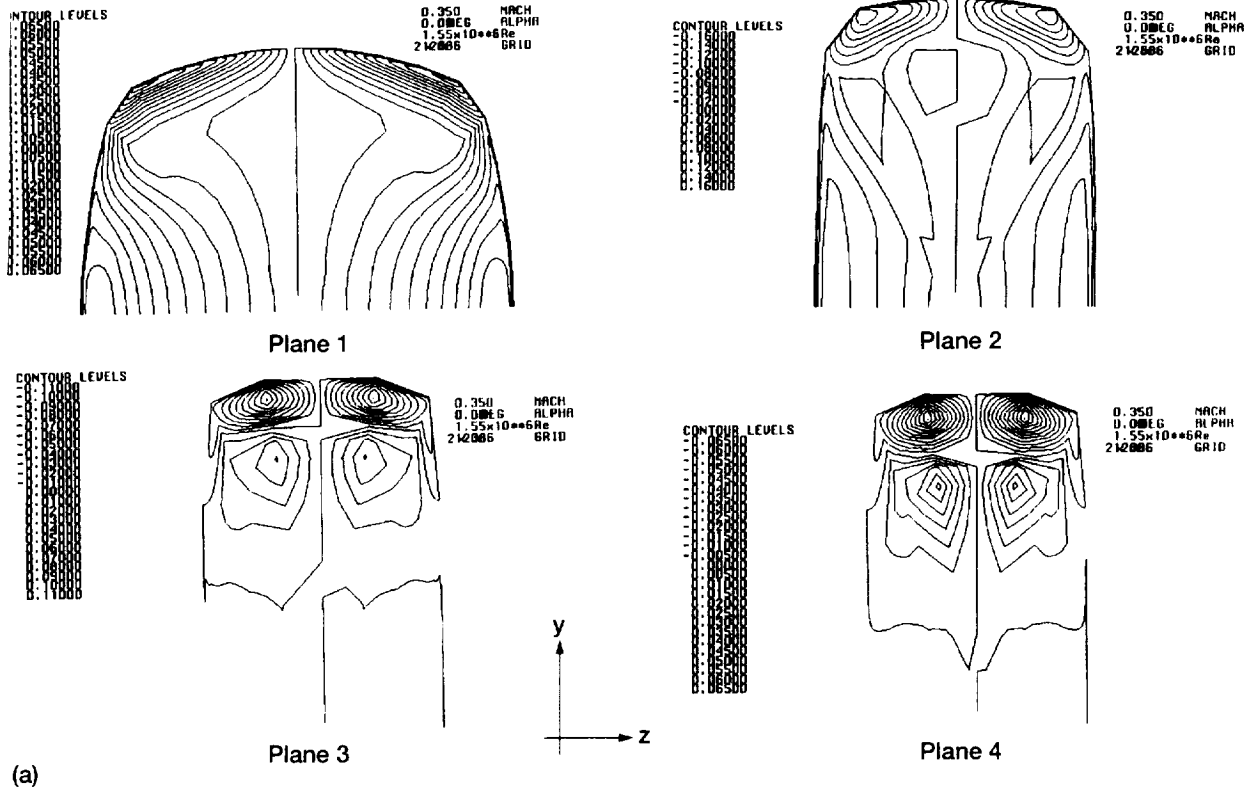


Figure 7.—Y-component of velocity. (a) Calculated results. (b) Experimental results (ref. 4).

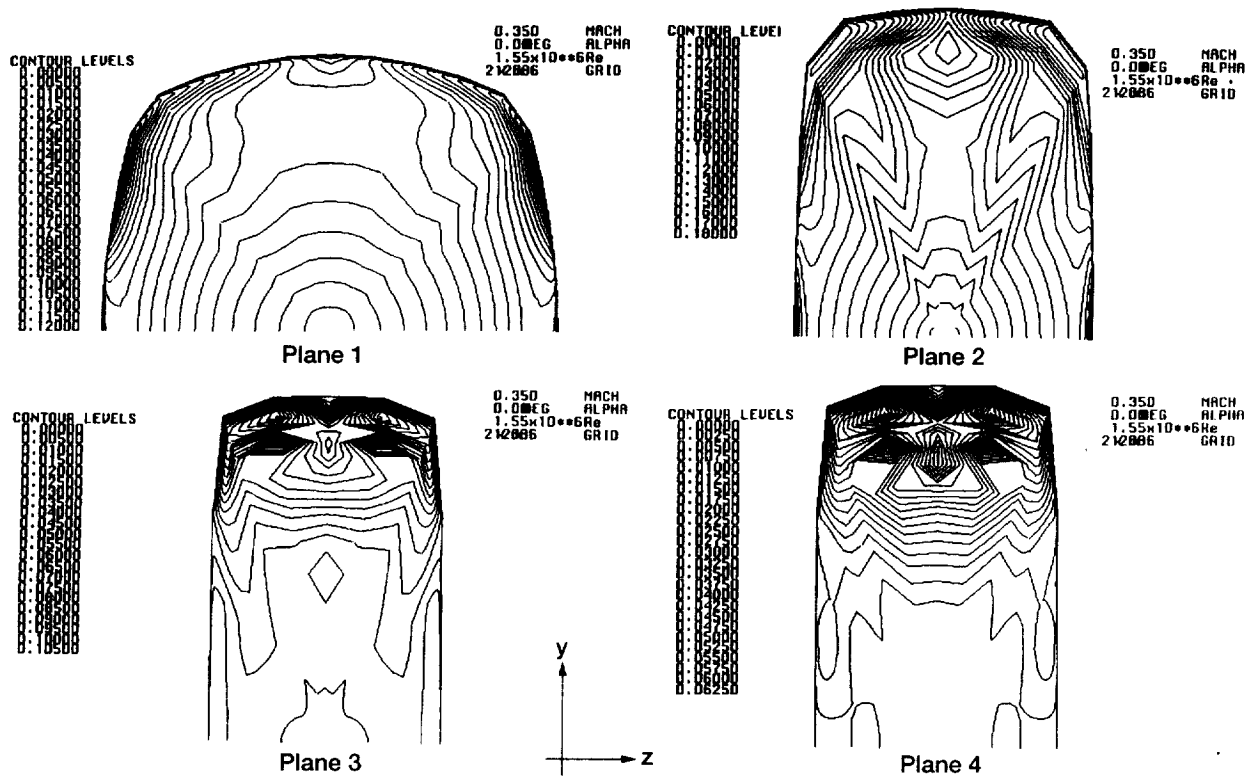


Figure 8.—Cross-flow velocity, calculated results.

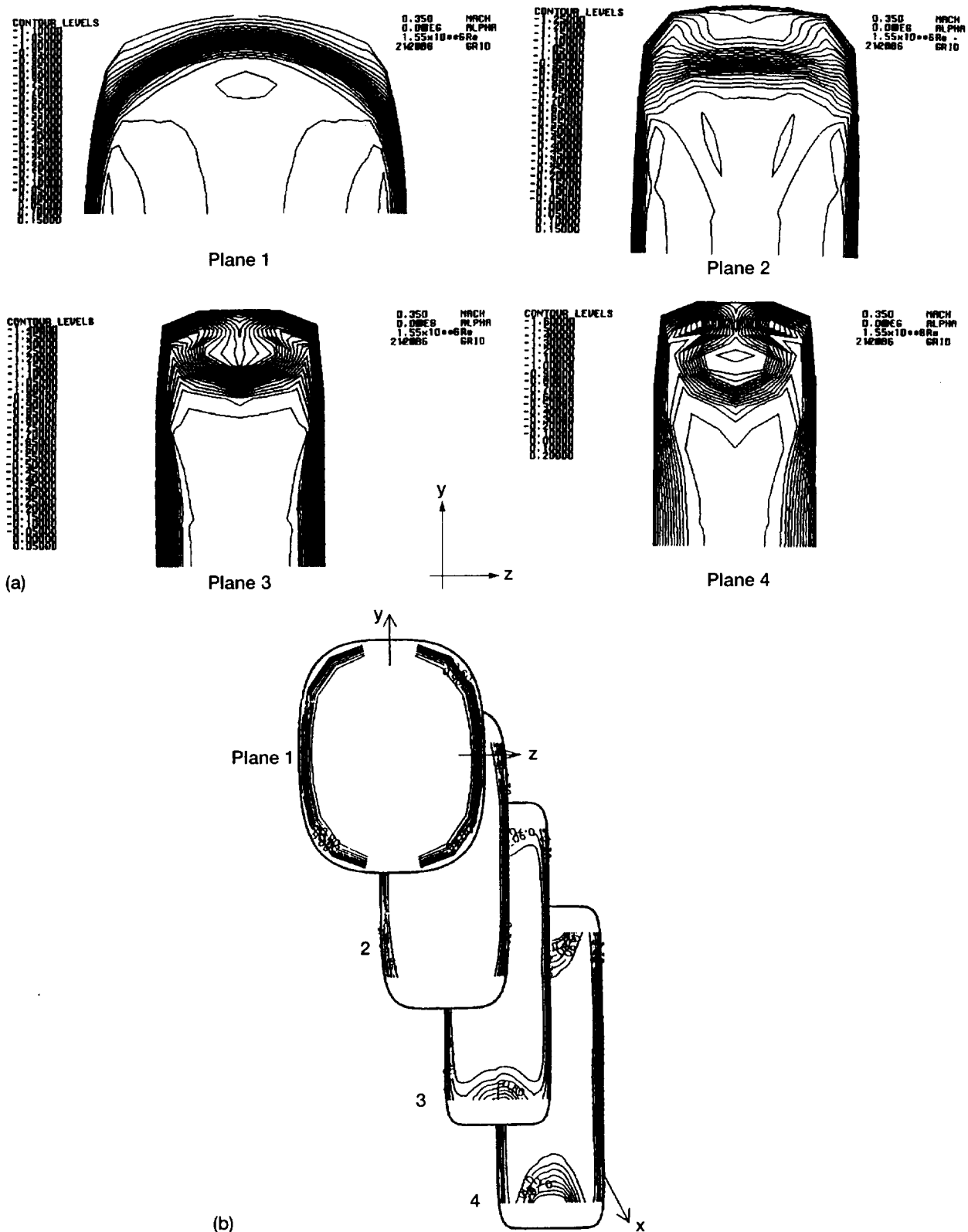


Figure 9.—Stagnation pressure coefficient. (a) Calculated results. (b) Experimental results (ref. 4).

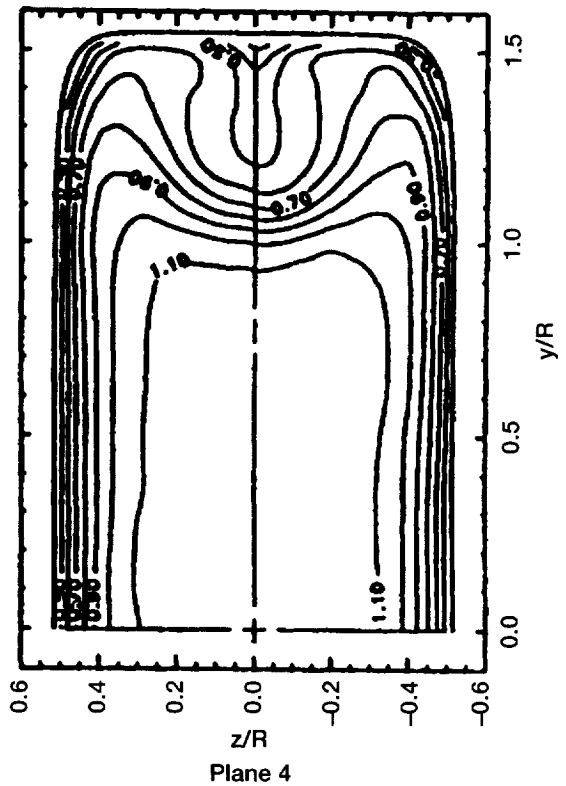
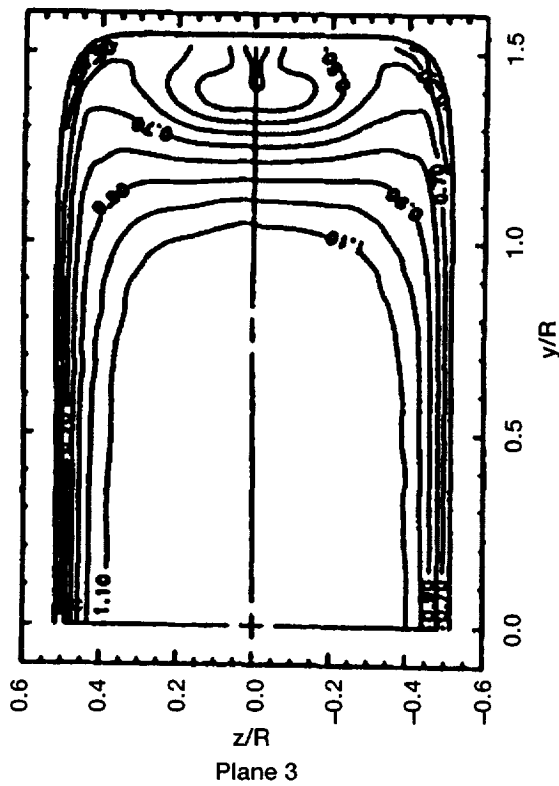
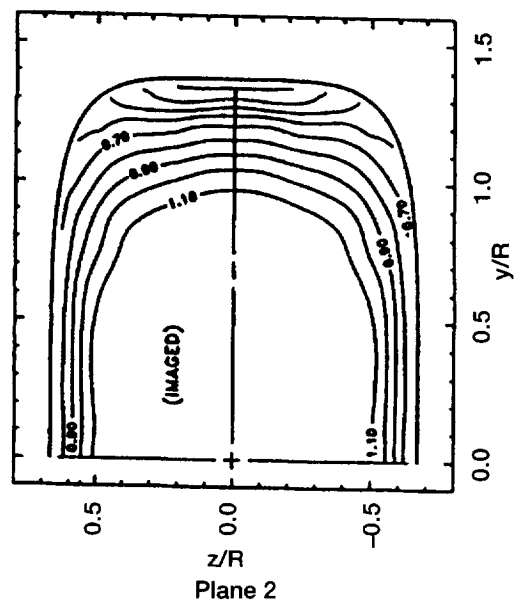
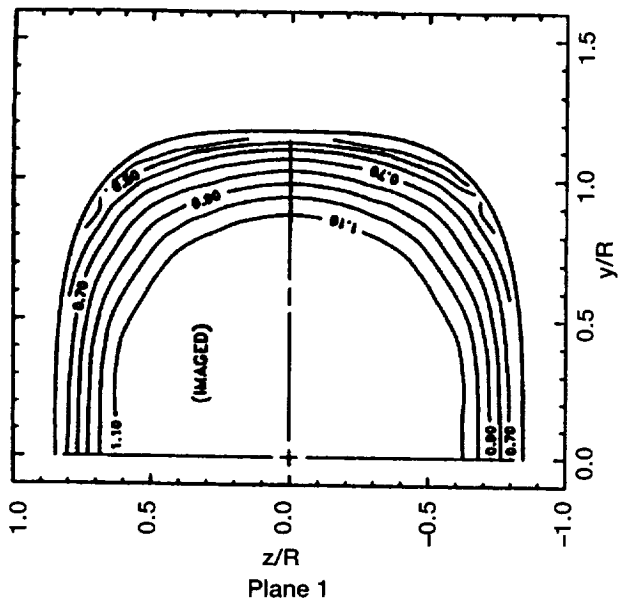
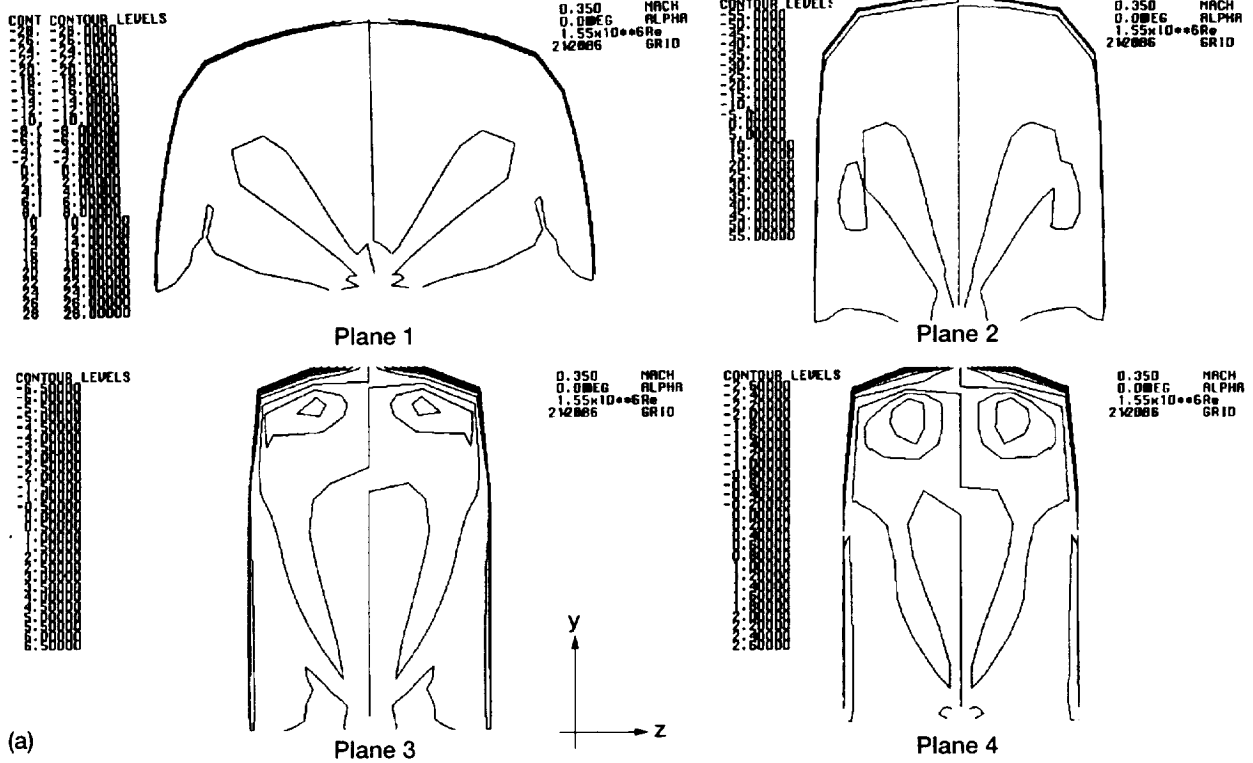
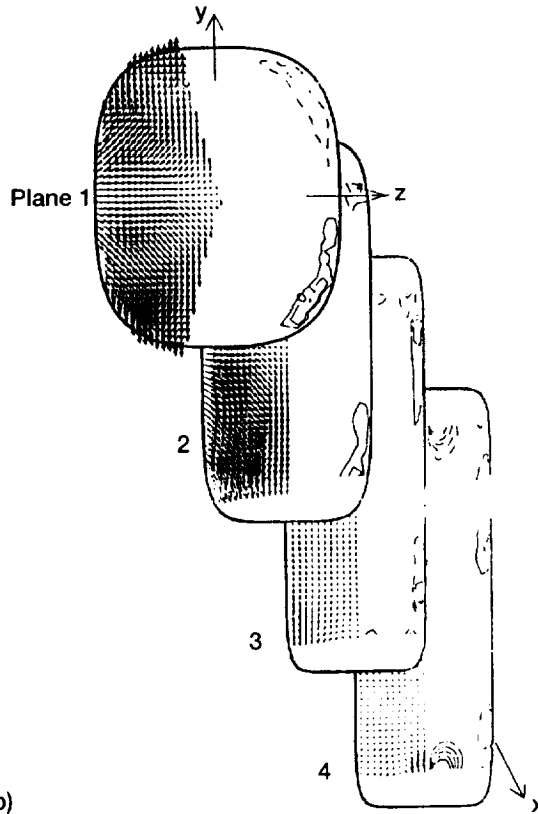


Figure 9.—Concluded. (c) Experimental results (ref. 3).



(a)



(b)

Figure 10.—Axial vorticity. (a) Calculated results. (b) Experimental results (ref. 4).

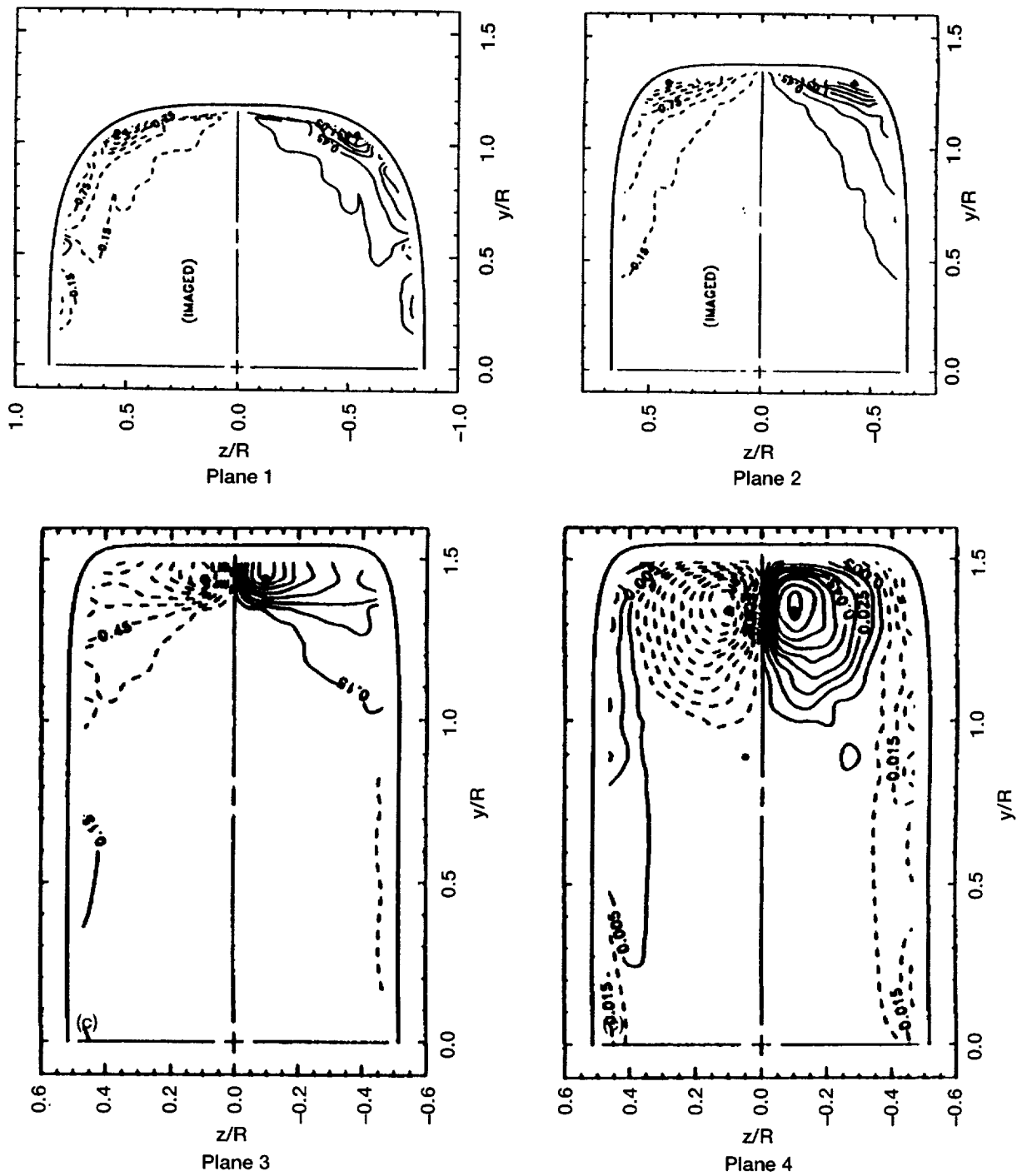


Figure 10.—Concluded. (c) Experimental results (ref. 3).

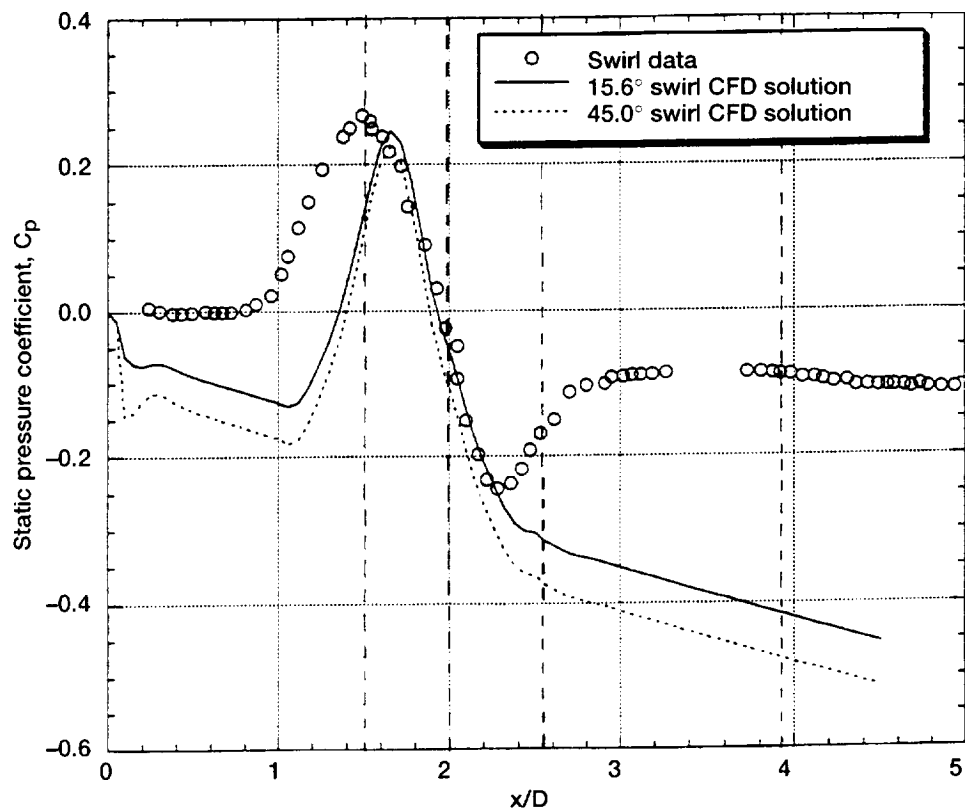


Figure 11.—Axial variation of static pressure coefficient, inlet swirl.

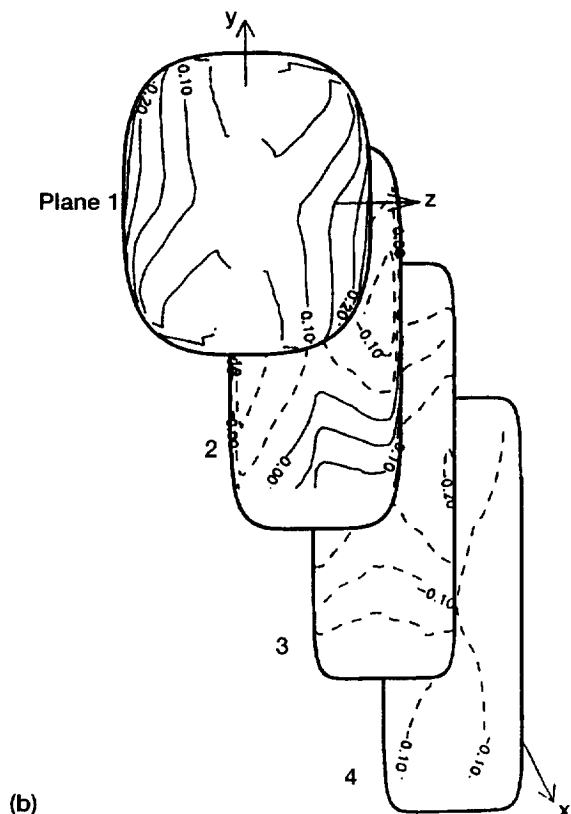
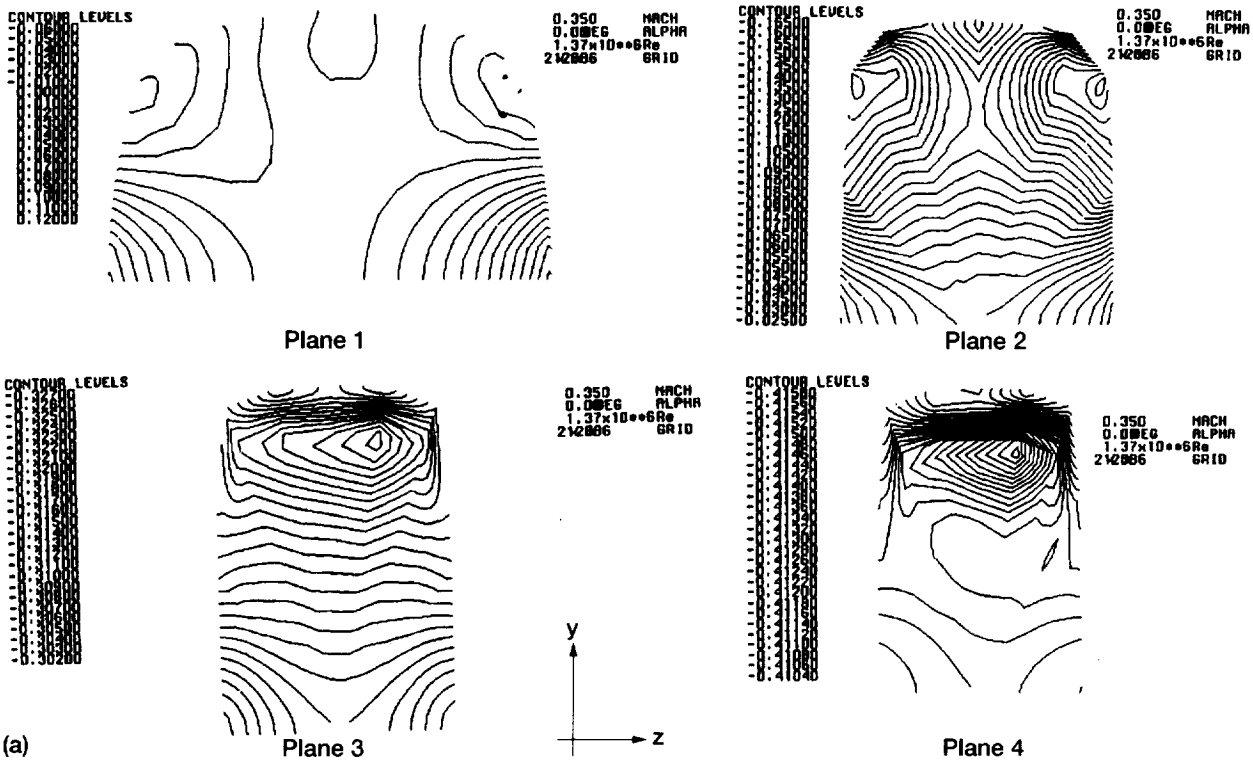


Figure 12.—Static pressure coefficient, 15.6° inlet swirl. (a) Calculated results. (b) Experimental results (ref. 4).

CONTOUR LEVELS

-0.46000
-0.45000
-0.44000
-0.43000
-0.42000
-0.41000
-0.40000
-0.39000
-0.38000
-0.37000
-0.36000
-0.35000
-0.34000
-0.33000
-0.32000
-0.31000
-0.30000
-0.29000
-0.28000
-0.27000
-0.26000
-0.25000
-0.24000
-0.23000
-0.22000
-0.21000
-0.20000
-0.19000
-0.18000
-0.17000
-0.16000
-0.15000
-0.14000
-0.13000
-0.12000
-0.11000
-0.10000
-0.09000
-0.08000
-0.07000
-0.06000
-0.05000
-0.04000
-0.03000

0.350 MACH
0.00EG ALPHA
1.37x10**6Re
212886 GRID

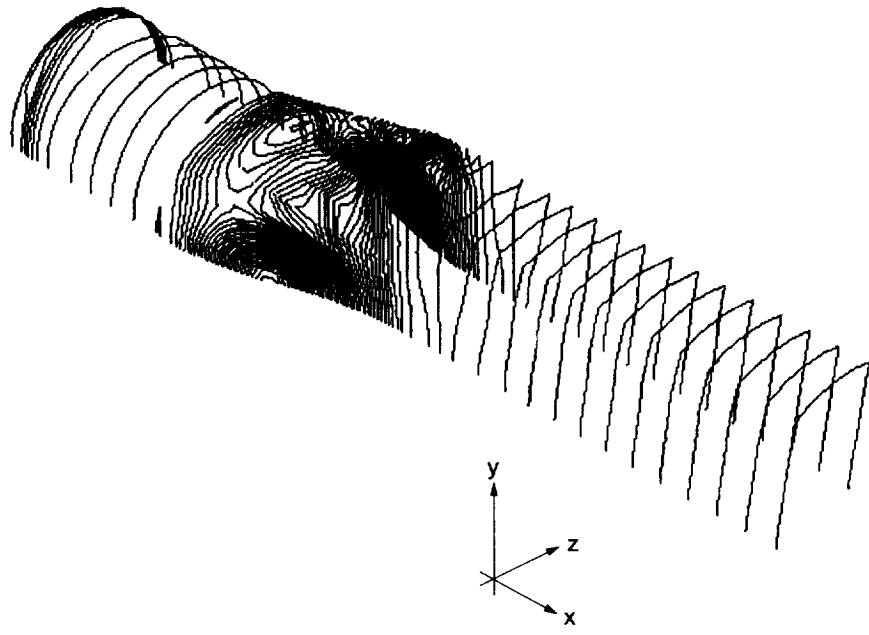


Figure 13.—Isometric view of static pressure coefficient, calculated results, 15.6° inlet swirl.

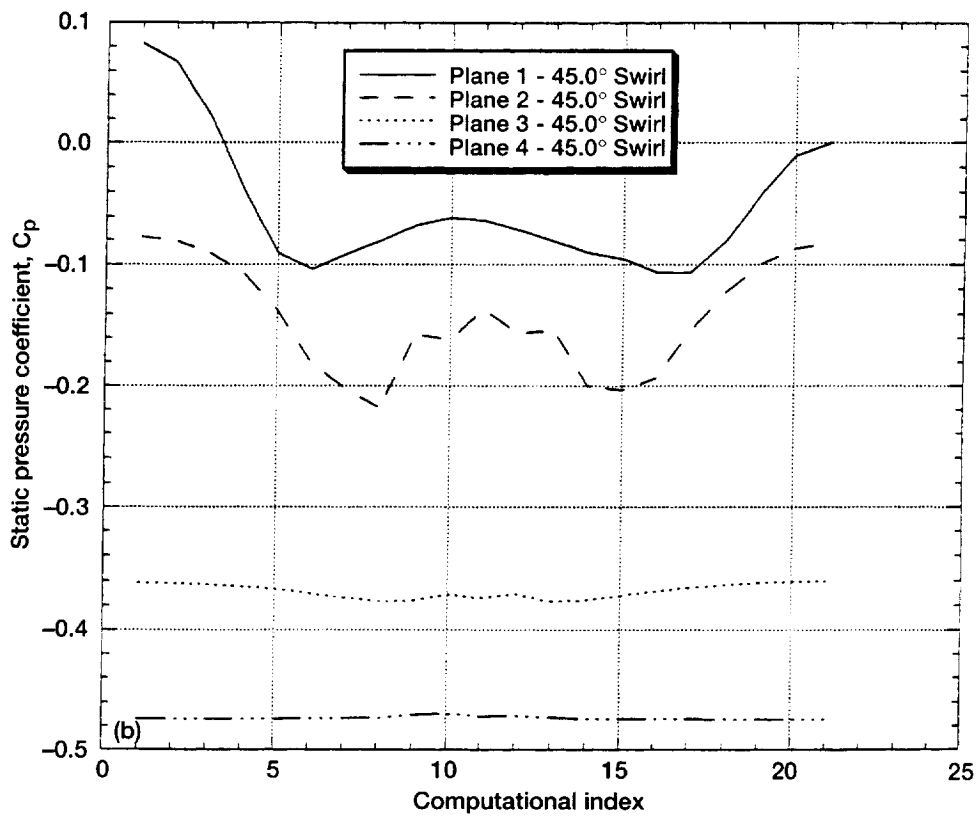
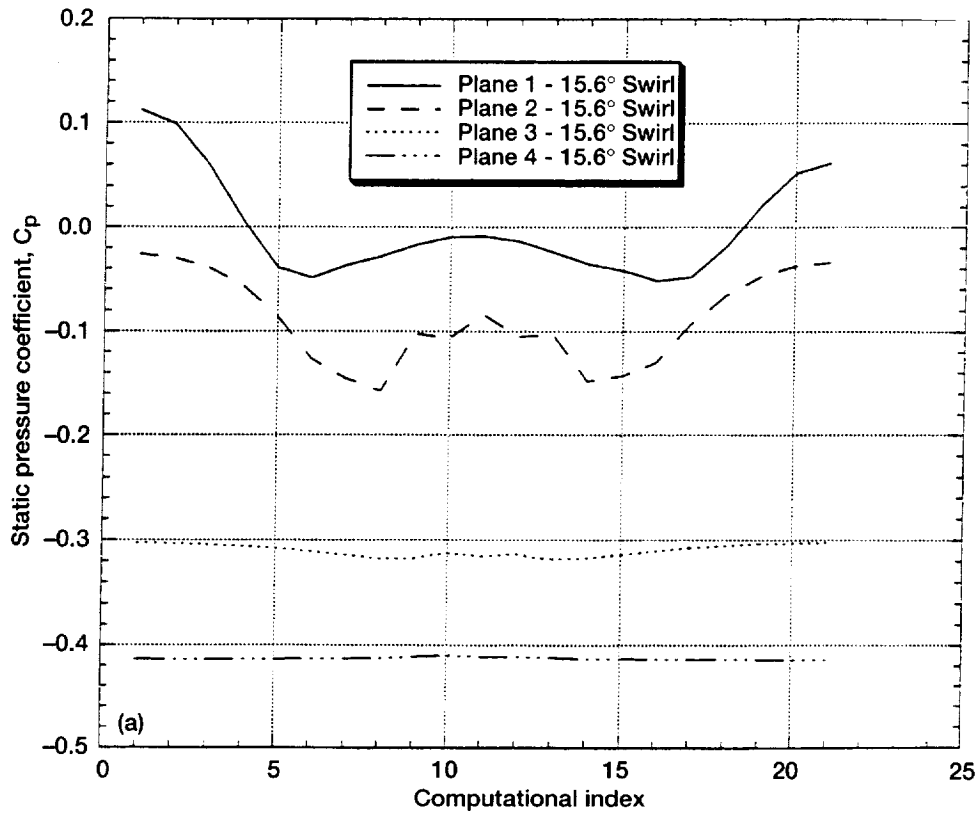


Figure 14.—Peripheral variation of static pressure coefficient. (a) 15.6° inlet swirl. (b) 45.0° inlet swirl.

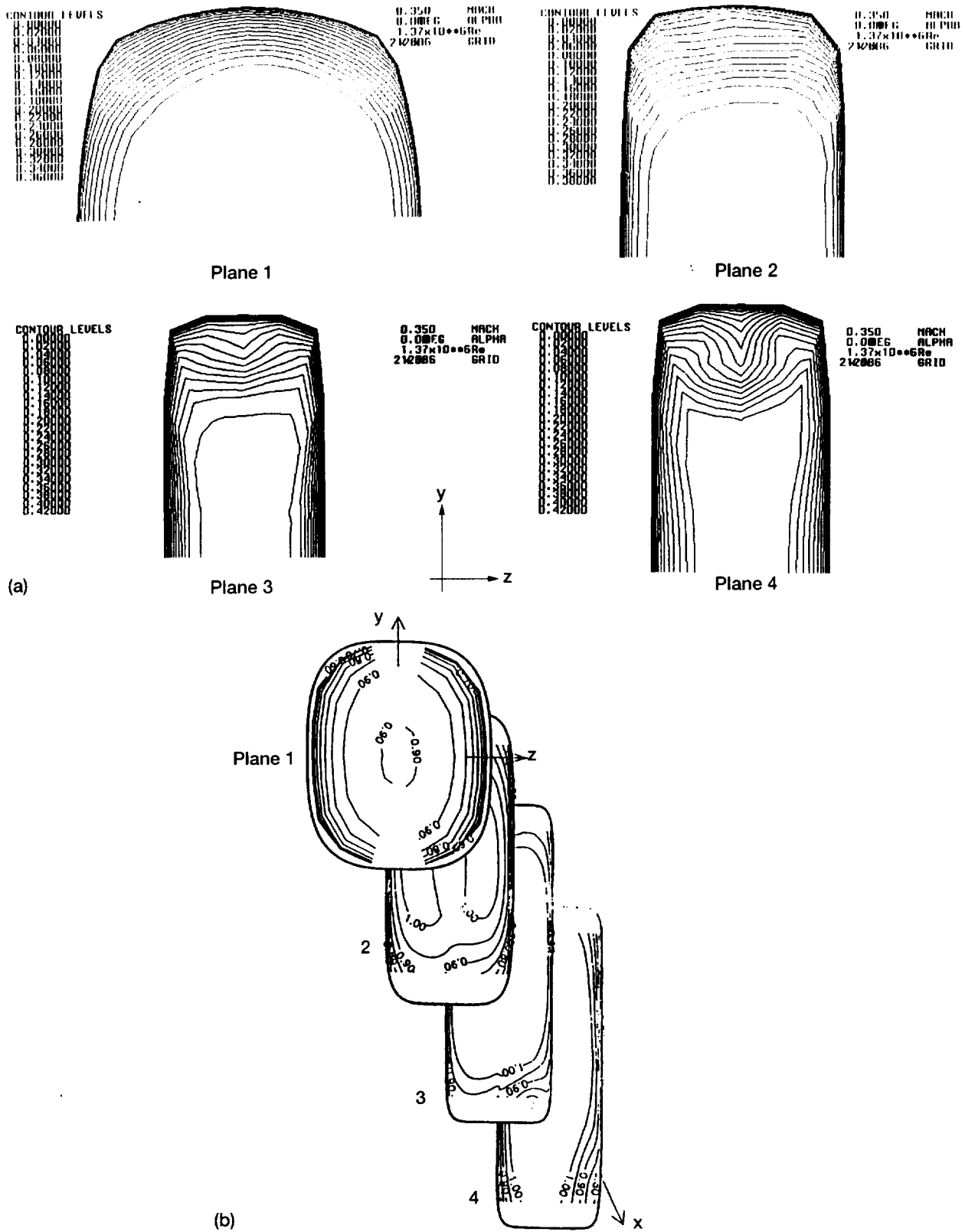


Figure 15.—Axial velocity, 15.6° inlet swirl. (a) Calculated results. (b) Experimental results (ref. 4).

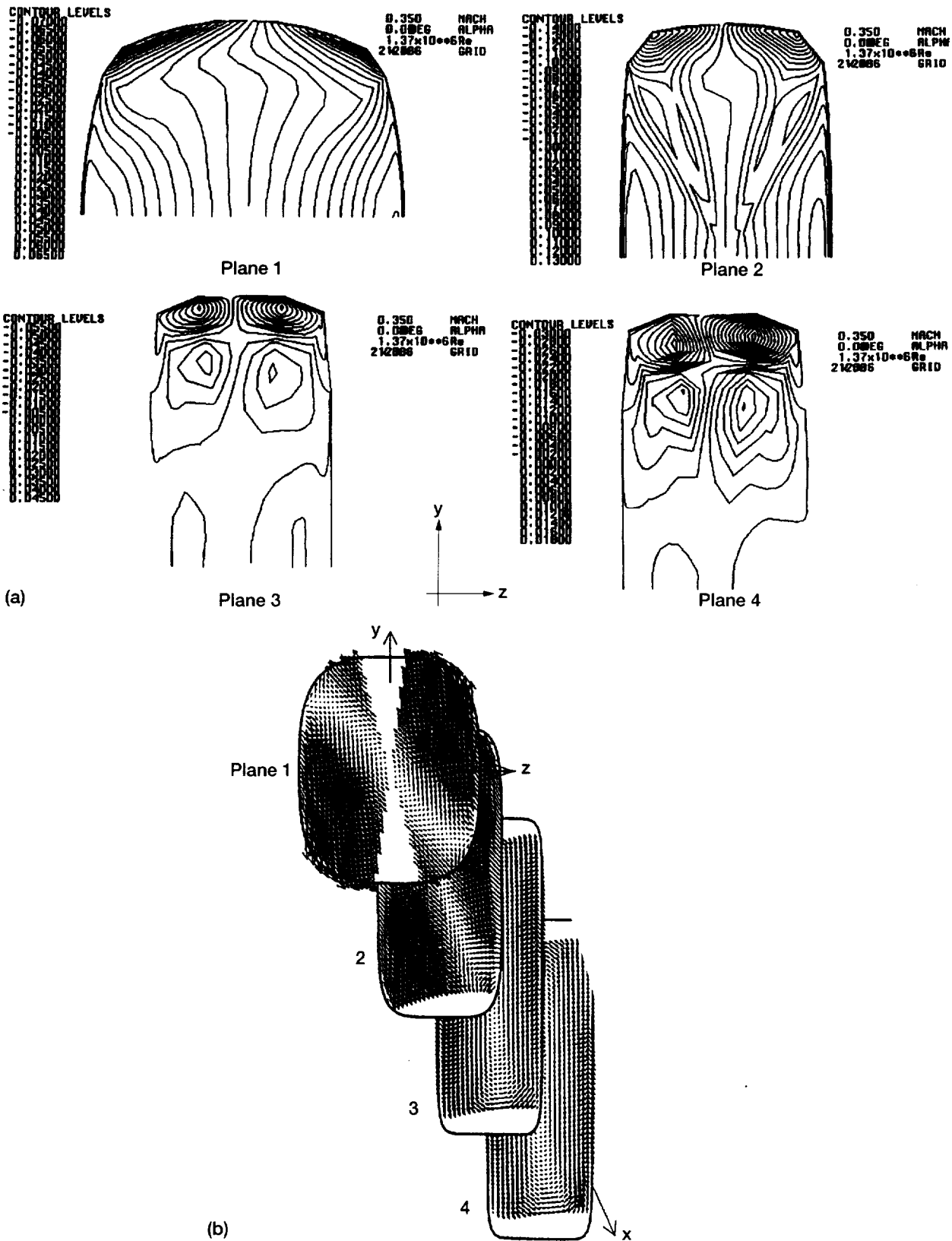


Figure 16.—Y-component of velocity, 15.6° inlet swirl. (a) Calculated results. (b) Experimental results (ref. 4).

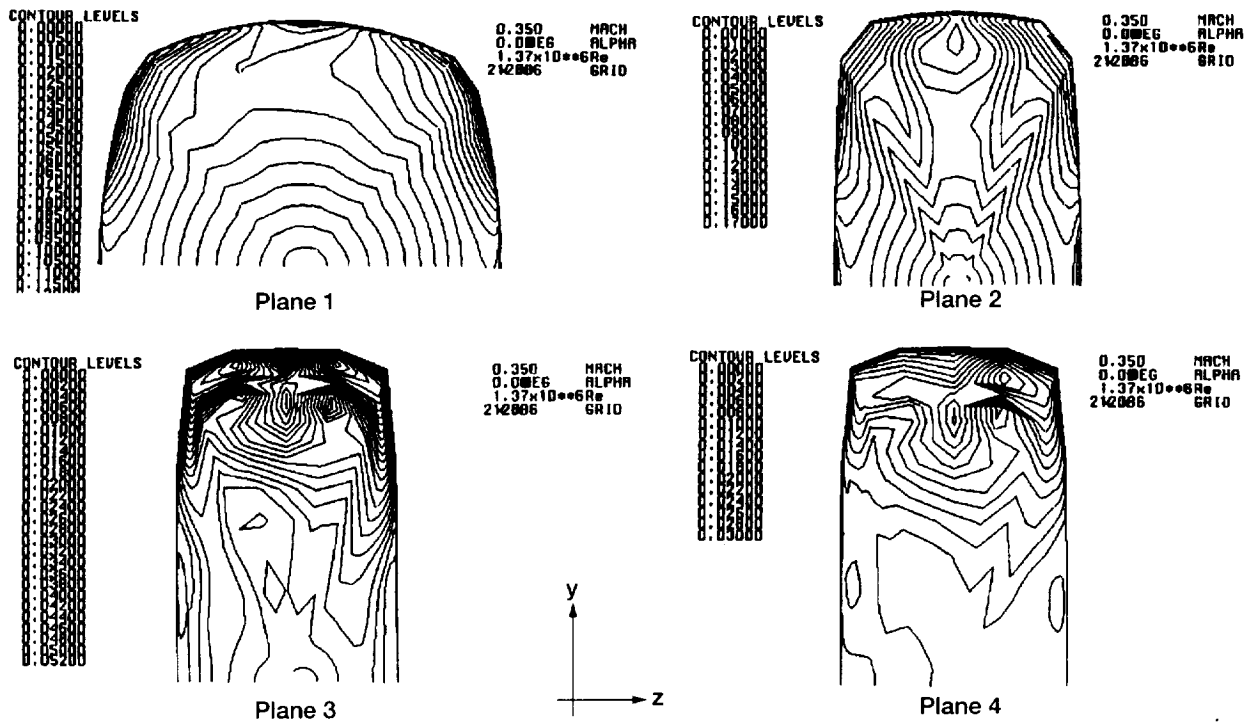
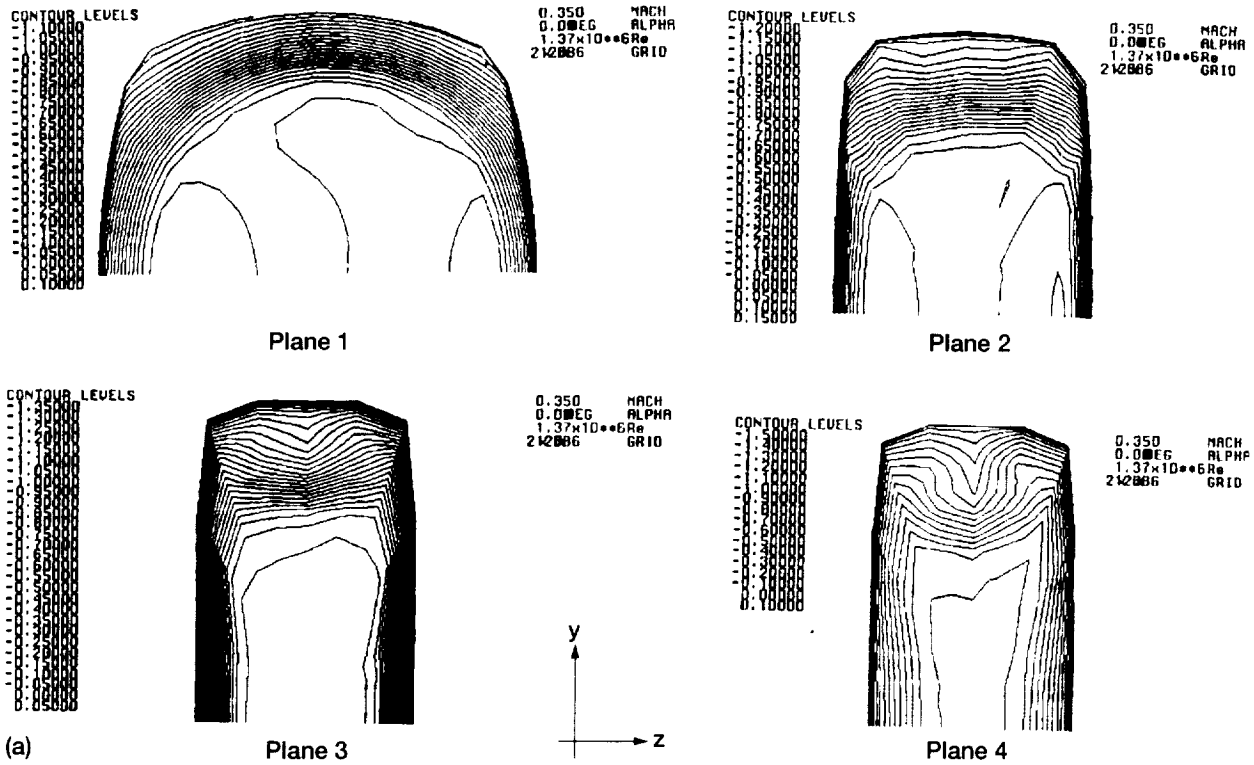
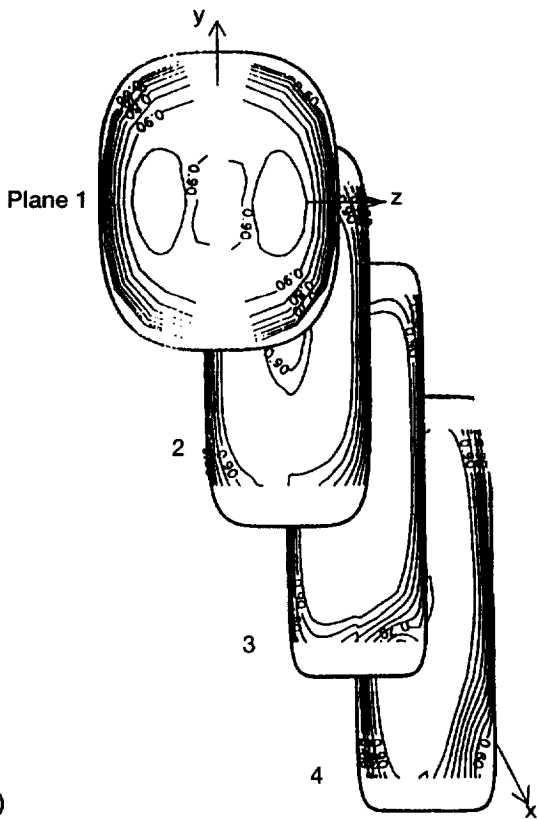


Figure 17.—Cross-flow velocity, 15.6° inlet swirl



(a)



(b)

Figure 18.—Stagnation pressure coefficient, 15.6° inlet swirl. (a) Calculated results. (b) Experimental results (ref. 4).

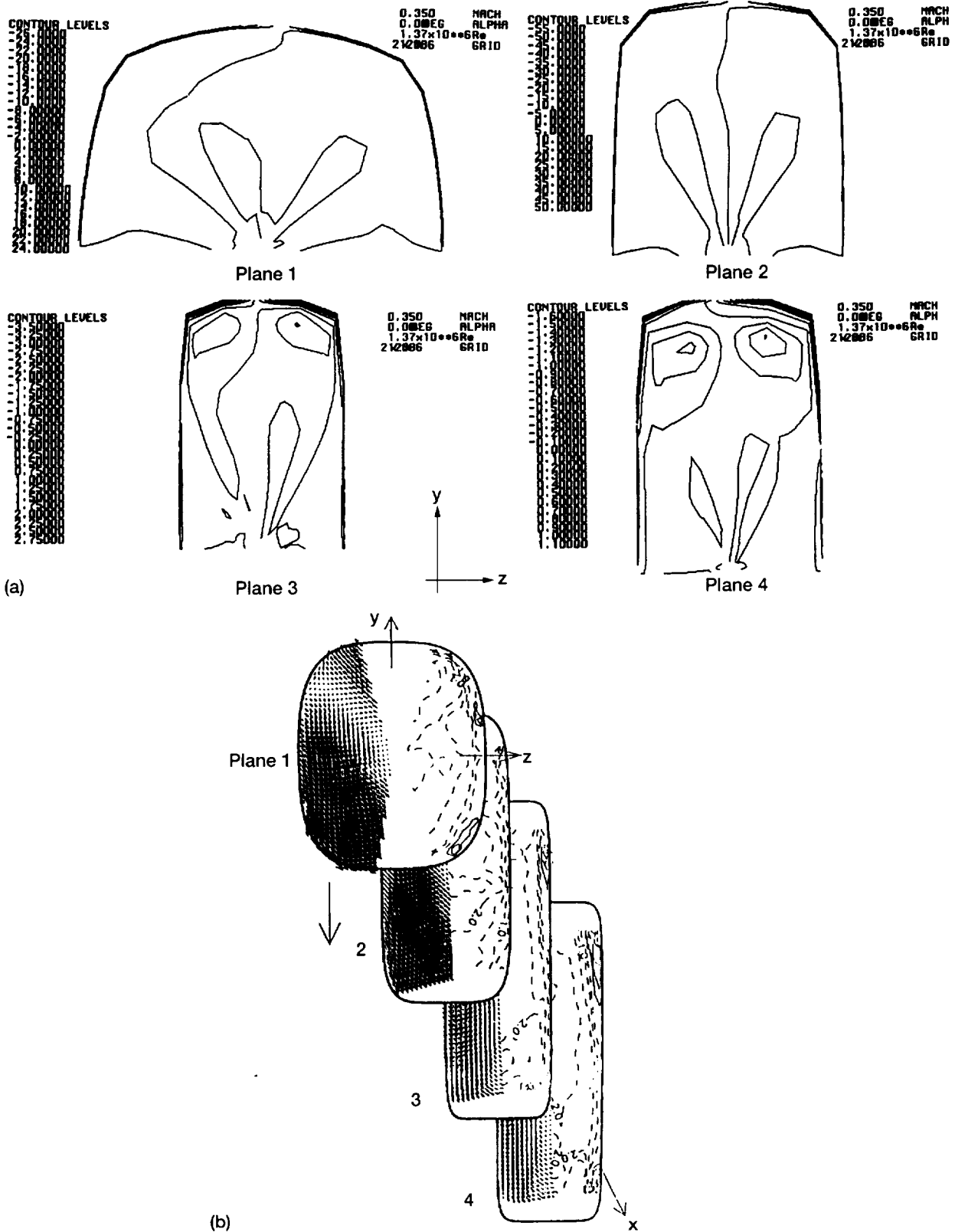


Figure 19.—Axial vorticity, 15.6° inlet swirl. (a) Calculated results. (b) Experimental results (ref. 4).

| REPORT DOCUMENTATION PAGE | | | Form Approved OMB No. 0704-0188 | |
|--|--|--|---|--|
| Public reporting burden for this collection of information is estimated to average 1 hour per response, including the time for reviewing instructions, searching existing data sources, gathering and maintaining the data needed, and completing and reviewing the collection of information. Send comments regarding this burden estimate or any other aspect of this collection of information, including suggestions for reducing this burden, to Washington Headquarters Services, Directorate for Information Operations and Reports, 1215 Jefferson Davis Highway, Suite 1204, Arlington, VA 22202-4302, and to the Office of Management and Budget, Paperwork Reduction Project (0704-0188), Washington, DC 20503. | | | | |
| 1. AGENCY USE ONLY (Leave blank) | 2. REPORT DATE October 1999 | 3. REPORT TYPE AND DATES COVERED Technical Memorandum | | |
| 4. TITLE AND SUBTITLE Application of the RNS3D Code to a Circular-Rectangular Transition Duct With and Without Inlet Swirl and Comparison With Experiments | | | 5. FUNDING NUMBERS WU-523-61-13-00 | |
| 6. AUTHOR(S) Richard H. Cavicchi | | | | |
| 7. PERFORMING ORGANIZATION NAME(S) AND ADDRESS(ES) National Aeronautics and Space Administration John H. Glenn Research Center at Lewis Field Cleveland, Ohio 44135-3191 | | | 8. PERFORMING ORGANIZATION REPORT NUMBER E-11828 | |
| 9. SPONSORING/MONITORING AGENCY NAME(S) AND ADDRESS(ES) National Aeronautics and Space Administration Washington, DC 20546-0001 | | | 10. SPONSORING/MONITORING AGENCY REPORT NUMBER NASA TM-1999-209394 | |
| 11. SUPPLEMENTARY NOTES Responsible person, Richard H. Cavicchi, NASA Glenn Research Center, organization code 5850, (216) 433-5873. | | | | |
| 12a. DISTRIBUTION/AVAILABILITY STATEMENT Unclassified - Unlimited Subject Categories: 02 and 34 This publication is available from the NASA Center for AeroSpace Information. (301) 621-0390. | | | 12b. DISTRIBUTION CODE Distribution: Nonstandard | |
| 13. ABSTRACT (Maximum 200 words) Circular-rectangular transition ducts are used between engine exhausts and nozzles with rectangular cross sections that are designed for high performance aircraft. NASA Glenn Research Center has made experimental investigations of a series of circular-rectangular transition ducts to provide benchmark flow data for comparison with numerical calculations. These ducts are all designed with superellipse cross sections to facilitate grid generation. In response to this challenge, the three-dimensional RNS3D code has been applied to one of these transition ducts. This particular duct has a length-to-inlet diameter ratio of 1.5, and an exit-plane aspect ratio of 3.0. The inlet Mach number is 0.35. Two GRC experiments and the code were run for this duct without inlet swirl. One GRC experiment and the code were also run with inlet swirl. With no inlet swirl the code was successful in predicting pressures and secondary flow conditions, including a pair of counter-rotating vortices at both sidewalls of the exit plane. All these phenomena have been reported from the two GRC experiments. However, these vortices were suppressed in the one experiment when inlet swirl was used; whereas the RNS3D code still predicted them. The experiment was unable to provide data near the sidewalls, the very region where the vortices were predicted. | | | | |
| 14. SUBJECT TERMS Ducts; Circular-retangular transition ducts; Ducts with super-elliptic cross sections; Inlet swirl; Turbulent flow; Application of 3-D Navier Stokes code | | | 15. NUMBER OF PAGES 33 | |
| | | | 16. PRICE CODE A03 | |
| 17. SECURITY CLASSIFICATION OF REPORT Unclassified | 18. SECURITY CLASSIFICATION OF THIS PAGE Unclassified | 19. SECURITY CLASSIFICATION OF ABSTRACT Unclassified | 20. LIMITATION OF ABSTRACT | |

